Silicon Nanotexture Surface Area Mapping Using Ultraviolet Reflectance

Giuseppe Scardera ⬤, David N. R. Payne, Muhammad Umair Khan, Yu Zhang, Anastasia Soeriyadi ⬤, Shuai Zou, Daqi Zhang, Rasmus Schmidt Davidsen ⬤, Ole Hansen ⬤, Bram Hoex ⬤, and Malcolm David Abbott ⬤

Abstract—**The enhanced surface area of silicon nanotexture is an important metric for solar cell integration as it affects multiple properties including optical reflectance, dopant diffusion, and surface recombination. Silicon nanotexture is typically characterized by its surface-area-to-projected-area ratio or enhanced area factor (EAF). However, traditional approaches for measuring EAF provide limited statistics, making correlation studies difficult. In this article, silicon's dominant ultraviolet reflectance peak, R(E2), which is very sensitive to surface etching, is applied to EAF spatial mapping. A clear decay correlation between R(E2) and EAF is shown for multiple textures created using reactive ion etching and metal catalyzed chemical etching. This correlation is applied to R(280 nm) reflectance mapping to yield accurate, high-resolution full-wafer EAF spatial mapping of silicon nanotextures. R(280 nm) mapping is also shown to be sensitive enough to correlate the impact of nanotexture spatial variation on post-diffusion sheet resistance. Finite-difference time-domain simulations of several nanoscale pyramid textures confirm a decay band for R(E2) versus EAF, consistent with our measurements. We suggest that R(E2) mapping may prove useful for other silicon nanotexture properties and applications where EAF is important.**

Index Terms—**Black silicon (B-Si), silicon nanotexture, spatial mapping, surface area, ultraviolet (UV) reflectance.**

I. INTRODUCTION

THE enhanced surface area of nanotextured silicon and "black silicon" (B-Si) are of great interest for various applications including lithium battery anodes [1], [2], photocathodes for photoelectrochemical hydrogen production [3], [4], and ultralow reflectance for photovoltaics [5], [6]. However,

the integration of low reflectance nanotextured B-Si into solar cells is complicated by the increased recombination losses also attributed to the enhanced surface area [7]. B-Si enhanced surface area is typically characterized by the lateral-surface-area-to-projected-area ratio, referred to here as the enhanced area factor (EAF). While there are various methods for creating B-Si, with feature dimensions spanning from the nano to micron scale, EAF typically increases with increased etching [7]–[12]. Multiple key parameters have been shown to be sensitive to B-Si EAF. The average reflectance (weighted against the AM1.5 solar spectrum) has been shown to decrease with increasing EAF for various B-Si texture conditions [7], [8], [12]. Increasing effective recombination velocity with increasing EAF has been reported for B-Si textures [7], [8] and effective minority carrier lifetime has also been shown to decrease with increasing EAF [12]. Silicon nanotexture enhanced phosphorus doping, observed as lower sheet resistance, has been readily attributed to the enhanced surface area [7]–[10], [13]–[15] although we have also recently reported on the role of surface-to-volume ratio or specific surface area [11].

Correlation studies of EAF to other key parameters tend to rely on limited statistics as there is no convenient method to monitor its spatial variation across an entire wafer. Silicon nanotexture and B-Si surface area has been characterized in various ways including indirectly via etched thickness using gravimetric measurements [10], calculated from a combined oxidation-gravimetric method [7], calculated from scanning electron microscopy (SEM) images [8], [12], or measured directly using atomic force microscopy (AFM) [9], [11], [15]. However**,** gravimetric methods only provide a single surface area (or surface-area-related) value for an entire wafer, whereas microscopy techniques sample a very small region (on the order of 100 μm^2).

In order to enable full-wafer silicon nanotexture monitoring with significant statistics, we propose making use of a fundamental silicon ultraviolet (UV) reflectance peak, which is sensitive to surface nanoetching, and can be extended to a 2-D scan. The reflectance spectrum for crystalline silicon exhibits two distinct peaks in the UV range. One peak, referred to as the E1 peak, R(E1), is typically observed at $\sim$3.4 eV ($\sim$365 nm) [16]–[18]. The more dominant peak, referred to as the E2 peak, R(E2), is typically observed in the range of $\sim$4.5–4.6 eV ($\sim$275–270 nm) [16]–[18], but has also been reported at $\sim$4.3 eV ($\sim$ 288 nm) [19]. Distinct E1 and E2 peaks also appear in silicon's other relevant optical spectra like the absorption coefficient [16], [20]
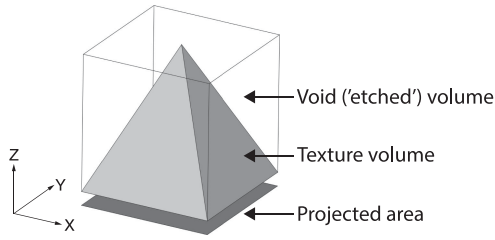
Fig. 1. Schematic of a square-based pyramid unit texture feature with void volume, texture volume, and projected area indicated.

and the imaginary part of both the refractive index [16], [20] and dielectric function [20], [21]. These peaks are associated with direct transitions at critical points in silicon's energy band structure, which correspond to points and lines of symmetry in silicon's first Brillouin zone in reciprocal space [22]. The E1 peak has been associated with the zone center point Γ [23], the edge point L [24], or along the $<111>$ axes (Λ) [25]. E2 has been associated with edge point X [19], [23], [25], near X along the $<100>$ axes (Δ) [26], or along the $<110>$ axes (Σ) [22], [24]. While the assignments of these peaks to exact critical points are not clearly defined [22], they do appear to serve as a fundamental silicon "fingerprint." The E1 and E2 peaks have been shown to be sensitive to silicon material quality and the E2 peak in particular to surface etching. The offset between R(E1) and R(E2) has been used to monitor the crystallinity of thin silicon films [27], [28]. R(E2) has been used to monitor silicon surface roughness [19] and has also been shown to clearly trend with porosity for electrochemically etched porous silicon [21]. It is worth noting that the R(E2) peak remains clearly detectable for ultralow reflectance B-Si achieved with aggressive etching [29], which is consistent with the fundamental nature of this peak. Similarly, the peak in the imaginary part of the pseudodielectric function, measured with spectroscopic ellipsometry, has been shown to be sensitive to microscopic surface roughness, described as a "form of density deficit" [30].

Such results indicate that E2 optical spectra peaks like R(E2) are very sensitive to the amount of etched silicon, which is related to a texture's void volume (i.e., "density deficit"). The relation to void volume is apparent when considering the typical gravimetric measurement employed to monitor an etching process. The total etched thickness T_{etch} is determined by measuring the pre-etching and post-etching wafer masses (M_{pre} and M_{post}, respectively) and then dividing the difference by the volumetric density ρ and projected wafer area A. T_{etch} is related to the texture void volume V_{void} via

$$T_{etch} = (M_{pre} - M_{post})/A\rho$$
$$= (V_{pre}\,\rho - V_{post}\,\rho)/A\rho = V_{void}/A$$

where V_{pre} and V_{post} are the pre-etching and post-etching wafer volumes, respectively. We refer here to V_{void}/A as the void-volume-per-projected area (VPA). Consider the schematic of a square base pyramid unit texture feature shown in Fig. 1. The void ("etched") volume denotes the nontexture volume within the cuboid defined by the square base and height dimensions of the pyramid. For a given etching process, the EAF is expected to

increase with increasing VPA. As the etched amount (or etched thickness) is related to texture surface area, we propose that R(E2) should be well suited for monitoring spatial variation in silicon nanotextures.

In this article, we demonstrate a clear correlation between R(E2) and EAF using a wide range of silicon nanotexture conditions prepared using reactive ion etching (RIE) and industrial metal catalyzed chemical etching (MCCE). EAF values are measured directly using AFM. We show that full-wafer reflectance maps at 280 nm are very sensitive to silicon nanotexture spatial variation and can be converted to accurate EAF spatial maps. We also demonstrate that R(E2) mapping provides enough statistics to monitor the impact of nanotexture variation on phosphorus diffusion. The R(E2) versus EAF relation is also studied using finite-difference time-domain (FDTD) simulations of nanoscale pyramid textures with a wide range of void volumes.

II. EXPERIMENT AND SIMULATION DETAILS

A. Silicon Nanotexturing and Characterization

In order to study the correlation between R(E2) and EAF, multiple silicon nanotexture conditions were prepared on monocrystalline wafers, so as to minimize texture spatial variation. Furthermore, reflectance spectra and EAF were measured at the same nominal locations on the samples. Two MCCE textures were prepared on, 156 × 156 mm, p-type monocrystalline Cz silicon wafers. A reference planar condition was also prepared on the same wafer type using an alkaline chemical polishing process. The MCCE texture process employed an initial damage removal step followed by an AgNO$_3$ solution nano-pitting step and a subsequent HF-HNO$_3$ step to create inverted texture features. More processing details are available in [31]. The two MCCE conditions were created by varying the post-nano-pitting etch time, with MCCE-1 corresponding to the longer etch time and MCCE-2 to the shorter.

RIE textures were applied to 350 μm thick, 4-in, round, double-side polished, Cz p-type (100) silicon wafers. RIE processing employed a noncryogenic RIE process using an SPTS Pegasus system employing an SF$_6$ and O$_2$ plasma with 3000 W coil power and 10 W platen power. Two different RIE recipe types were used: RIE A and RIE B. The RIE A process used a temperature of –20 °C, an SF$_6$:O$_2$ gas flow ratio of 7:10, and a total chamber pressure of 38 mTorr. Five RIE A texture conditions (RIE A-1 to A-5) were created by varying the plasma process time (4, 8, 10, 12, and 14 min). One RIE B condition was prepared using a temperature of 0 °C, O$_2$ and SF$_6$ flow rates of 76 and 74 sccm, respectively, a chamber pressure of 24 mTorr, and a 6-min plasma time. Etching settings for the MCCE and RIE conditions are listed in Table I.

Reflectance spectra around the R(E2) peak (250–300 nm) and for the visible-to-near-infrared range (400–1000 nm) were measured using a Perkin Elmer 1050 spectrophotometer equipped with an integrating sphere at an 8° angle of incidence to the normal. AFM scans were performed using a Bruker ICON in tapping mode with a TESPD diamond-like carbon coated silicon probe with a nominal tip radius of 18 nm. Scan areas of 10 μm by 10 μm using 512 line-scans were employed for MCCE and RIE

	Key process details	
Condition	Shared MCCE chemistry	Post-MCCE etch* relative duration
MCCE-1	AgNO₃ solution*	long
MCCE-2		short
	Shared plasma settings	Etch time [min]
RIE A-1	3000 W coil power	4
RIE A-2	10 W platen power	8
RIE A-3	SF₆:O₂ = 1.03	10
RIE A-4	-20 °C	12
RIE A-5	38 mTorr	14
RIE B	3000 W coil power	6
	10 W platen power	
	SF₆:O₂ = 0.7	
	0 °C	
	24 mTorr	

*See [31] for more details.

A samples. A scan area of 5 μm by 5 μm using 512 line-scans was employed for RIE B. Surface areas were determined using a triangulation method [32] within the Gwyddion software[33]. Void fraction versus depth was determined from cumulative height distributions, extracted from AFM scans, using Gwyddion [33] and employing Bearing ratio methodology [34]. The void fraction versus depth curve for each nanotexture condition was numerically integrated to get the integrated void fraction values, which serve as a relative indicator of the amount of etched silicon or void volume. A correlation between R(E2) and EAF was determined by fitting the data with an exponential decay function. A similar fit was also performed on corresponding data for R(550 nm) as a reference (as it represents the visible range midpoint). Texture morphology was also monitored with SEM images using a field-emission FEI NanoSEM 450.

B. Reflectance Mapping and Diffusion

In order to demonstrate EAF mapping capability, reflectance maps were performed on MCCE textured multicrystalline silicon (mc-Si) wafers with spatial variation associated with different grains. The ability to monitor the impact of such texture variation on a phosphorus diffusion process was also investigated. Two sets of MCCE textures were prepared on neighboring ("sistered"), 156.75 mm by 156.75 mm, p-type mc-Si wafers (two wafers per set), with condition MCCE-M1 receiving the longest post-nano-pitting etch time and condition MCCE-M2 the shortest. Both sets of wafers received an additional 2% KOH treatment for 30 s. This additional step further widened the openings of the inverted features and aided in accentuating spatial variation because of the anisotropic etch behavior for the different grain orientations. Reflectance maps were measured (on one wafer per set) using a PVTools LOANA system, equipped with an integrating sphere at an 8° angle of incidence to the normal, an x–y scanning stage, and using xenon and tungsten lamps as illumination sources. Note that a 0.3 mm gap between the integrating sphere and the wafer enables scanning. Unlike a laser-based reflectance tool, the LOANA allows for specific wavelength selection. UV reflectance mapping was

implemented at 280 nm (the lowest available wavelength), which is close to the wavelength for typical R(E2) peaks. Reflectance maps were also measured at a wavelength of 550 nm (midpoint of the visible range) as a reference. Full-wafer maps were performed using a 1 mm by 1 mm spot size and a 250 μm spatial resolution. It should be noted that such a spot size is significantly larger than that of a laser and, as such, limits the sharpness of the maps. In order to avoid any wafer edge reflectance artifacts, a 1 mm exclusion was implemented along the wafer perimeter, yielding 154.75 mm by 154.75 mm maps. Reflectance maps were converted into EAF maps by means of the correlation curves determined from the reflectance versus EAF for the monocrystalline B-Si samples described in Section II-A. In order to verify the accuracy of the reflectance methods, AFM scans were performed at the center of four different grain locations on the MCCE-M2 wafer and the extracted EAF values were compared with those determined from the R(280 nm) and R(550 nm) maps at the same nominal locations.

The remaining "sistered" multicrystalline MCCE wafers were subjected to a POCl₃ phosphorus diffusion using a Tempress TS8603 quartz tube furnace. The process employed a deposition step at 770 °C for 25 min with 400 sccm of POCl₃, 600 sccm of O₂, and 6.2 slm of N₂. This was followed by an 810 °C step for 30 min with 7.5 slm N₂ and a drive-in step at 880 °C for 40 min with 5 slm of O₂ and 2.5 slm of N₂. Sheet resistance was measured at 81 points across each wafer with an 8.7 mm edge exclusion using a Sunlab Sherrescan four-point probe. R(280 nm) and EAF values were extracted from the high-resolution maps at the same locations as those used for the post-diffusion four-point probe maps to allow for a direct comparison.

C. FDTD Simulations

In order to gain more insight into the relation between R(E2) and surface area for silicon nanotexture, we simulated ideal square nanopyramid textures spanning a wide range of EAF and VPA values. Simulations were carried out using the Lumerical 3-D electromagnetic simulator, utilizing the FDTD technique. For each nanopyramid geometry considered, a single pyramid was constructed on top of a bulk silicon substrate, the surface of which was in the *XY* plane (see Fig. 1). Si material was modeled using refractive index parameters from [22]. The simulation domain was designed using periodic boundaries in the *X* and *Y* directions and perfectly matched layers boundaries in the *Z*-direction. The periodic boundaries were positioned along the nanopyramid base dimensions, effectively modeling an infinite array of close-packed nanopyramids on an infinitely thick silicon substrate. A plane-wave source was positioned in air above the Si nanopyramid feature and directed toward the Si at normal incidence to the *XY* plane. The source was set to cover a wavelength range of 250–300 nm and a frequency-domain profile and power monitor were positioned behind the source to detect reflected light over the same wavelength range at a spectral resolution of 0.25 nm.
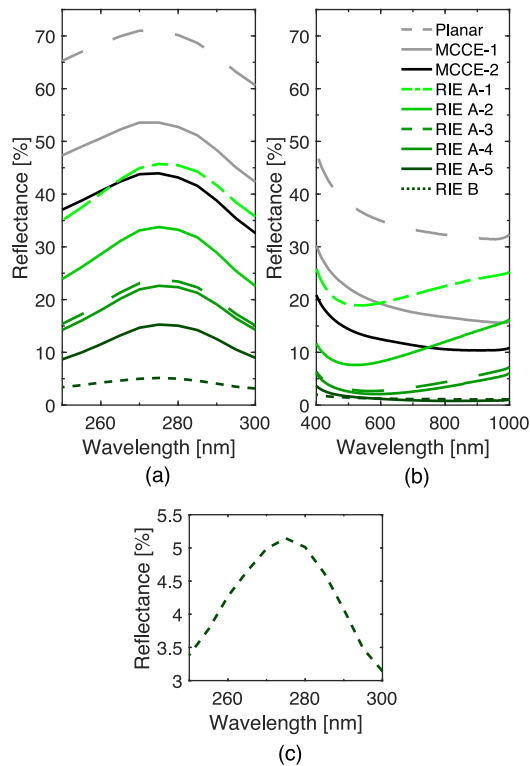
Fig. 2. Reflectance spectra for various MCCE and RIE nanotextured samples and a planar reference in the (a) UV regime centered around the R(E2) silicon peak and in the (b) visible-near-IR range. (c) Zoom-in of R(E2) peak for lowest reflectance condition (RIE B).
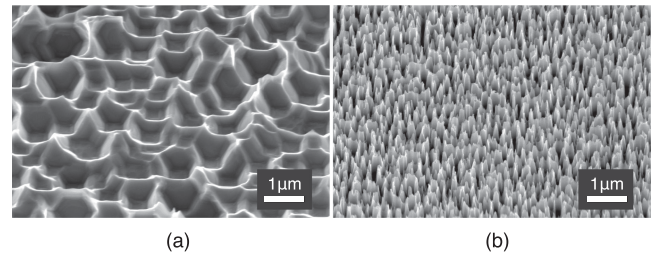

Fig. 3. SEM images, taken at a 45° tilt, of (a) the highest reflectance nanotexture condition (MCCE-1) and (b) the lowest nanotexture reflectance condition (RIE B).
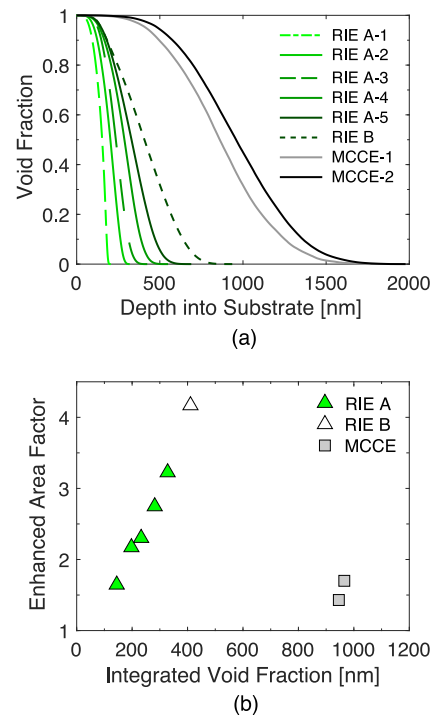

Fig. 4. (a) Void fraction versus depth into substrate extracted from AFM scans for all the nanotexture conditions. (b) Corresponding EAF versus integrated void fraction.

III. RESULTS AND DISCUSSION

A. Silicon Nanotexture Reflectance and EAF Correlations

The reflectance spectra for all the texture conditions, including the planar reference, are shown in Fig. 2. The R(E2) peaks for all the conditions occur at 275 nm except for RIE A-1 that occurs at 280 nm. It should be noted that the difference in reflectance between 275 and 280 nm is within ∼0.1% for all conditions. The R(E2) peaks for all conditions, shown in Fig. 2(a), are clearly offset across a wide range. The overall order of the reflectance spectra (i.e., from highest to lowest) is maintained up to approximately 600 nm, as shown in Fig. 2(b). The RIE A-1 to RIE A-5 spectra, shown in Fig. 2(b), exhibit distinct minima, with their location ranging from 530 to 825 nm, and varying upward slopes beyond the minima, except for RIE A-5, which has a slight downward slope. The reflectance for RIE B in Fig. 2(b) is relatively flat. The relative flattening of the reflectance spectra across the RIE conditions may be because of an increasing gradient refractive index, as observed for porous silicon [35]. The two MCCE spectra remain consistently offset from each other across the entire measured wavelength range. The significant changes in the RIE spectra result in the overall order of all the spectra to change above 600 nm. The zoom-in shown in Fig. 2(c) confirms that the R(E2) peak remains very clear even for the most aggressive condition.

Fig. 3(a) and (b) shows the SEM images (taken at a 45° tilt) for the highest and lowest reflectance nanotexture conditions, MCCE-1 and RIE B, respectively. The MCCE-1 condition

exhibits randomly distributed, low aspect ratio, submicron, inverted features. The RIE-B condition exhibits randomly distributed nanoscale, high aspect ratio, conical features.

Fig. 4(a) shows the void fraction versus depth into the substrate (starting from the highest texture point), extracted from AFM scans, for all the nanotexture conditions. The RIE A conditions exhibit increasing void fraction and maximum depths with increasing etch time, whereas RIE B exhibits the largest RIE void fraction and maximum depth. The MCCE conditions exhibit significantly larger void fractions and maximum depths compared with RIE. The shorter post-nano-pitting etch-back time condition (MCCE-2) exhibits the largest void fraction. The MCCE curves have more overlap compared with RIE and exhibit marginal changes.

Fig. 4(b) shows the corresponding EAF versus integrated void fraction [i.e., numerical integration of the curves shown in Fig. 4(a)] for all the nanotexture conditions. The RIE conditions span a wide range of EAF over a narrow range of integrated void
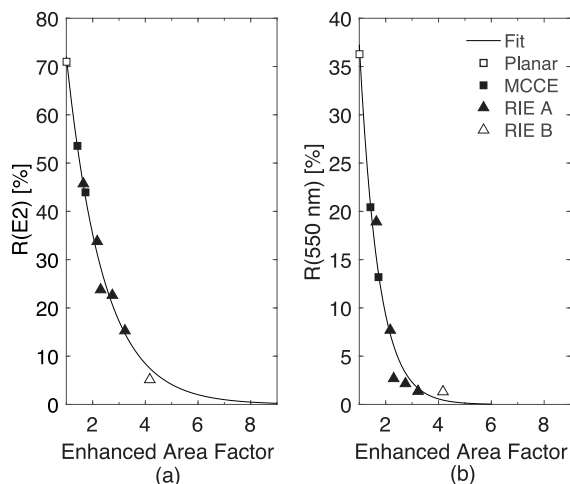
Fig. 5. (a) R(E2) and (b) R(550 nm) versus EAF for all texture conditions. Exponential decay fits to the data also shown.

Fig. 6. (a) R(280 nm) map and (b) R(550 nm) map (154.75 mm by 154.75 mm) of a multicrystalline wafer with MCCE-M2 texture. The corresponding EAF maps calculated using the correlation fits from Fig. 5 are shown in (c) and (d).

fraction. The RIE conditions also exhibit a clear relationship between EAF and the integrated void fraction, indicating that both the surface area and the relative void volume are increasing with increasing etch time. The MCCE conditions span a much smaller range of EAF, with marginal changes in integrated void fraction. Fig. 4(b) also confirms the nonuniqueness of EAF for a given VPA, as MCCE-2 exhibits a very similar EAF value as RIE A-1, despite the two textures having very different morphologies and relative void volumes. It should also be noted that the accuracy of the EAF values is limited by the ability of the AFM probe to resolve texture nano features. More specifically, we expect AFM to underestimate EAF values for deep, high aspect ratio features. The accuracy of higher EAF measurements may be improved with more advanced techniques like 3-D tomography [36].

Fig. 5(a) shows the R(E2) versus EAF plot for all the texture conditions. The R(E2) values exhibit a clear decay relation with EAF. The fit shown in Fig. 5(a) is an exponential function with a scale factor of 147.2, and a growth rate of –0.71. The fit yields an adjusted R^2 value of 0.987 and a root mean squared percentage error of 19.3%. The R(E2) values for the MCCE conditions align well with the RIE conditions. Fig. 5(b) shows the corresponding R(550 nm) versus EAF plot. The trend with EAF is less obvious than that exhibited by the R(E2) values. The offset between the higher EAF values is also less distinct. We note that while the overall order of the spectra is maintained at 550 nm, as shown in Fig. 2(b), the changing position of the spectra minima for the RIE conditions likely affects the relative offsets between R(550 nm) values for the higher EAF values. The fit shown in Fig. 5(b) is an exponential function with a scale factor of 150.1, and a growth rate of –1.39. The fit yields an adjusted R^2 value of 0.972 and a root mean squared percentage error of 58.5%. It is clear from Fig. 5 that R(E2) more clearly tracks with EAF than R(550 nm), especially for the higher EAF values. Furthermore, the exponential fit for the R(E2) curve approaches zero for an EAF value close to 9, whereas that for the R(550 nm) fit approaches zero for an EAF value close to 5. It is worth noting that EAF values as high as 5.2 [7] and 8.5 [8] have been reported for B-Si textures. The results in Fig. 5 suggest that R(E2) is
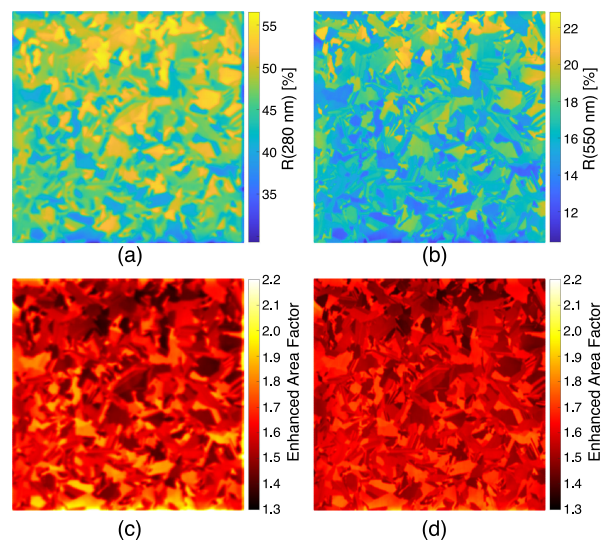
more sensitive to EAF. However, R(550 nm) does exhibit a clear trend with EAF for lower EAF values. Such a result combined with the consistent reflectance spectra offset for the two MCCE conditions shown in Fig. 2 may, at first glance, suggest that R(550 nm) may be suitable for monitoring variations for lower EAF conditions. In the following section, the higher sensitivity of R(E2) to EAF variation is verified by applying the correlations shown in Fig. 5 to R(280 nm) and R(550 nm) full-wafer maps of an MCCE textured mc-Si wafer, where the EAF values are below 2.2. It should be noted that the R(280 nm) values from Fig. 2(a) versus EAF yielded an exponential fit with negligible difference with the R(E2) relation shown in Fig. 5(a).

B. Reflectance and Surface Area Mapping

The R(280 nm) and R(550 nm) full-wafer maps for a mc-Si wafer with MCCE-M2 texture are shown in Fig. 6(a) and (b), respectively. While the same grains are clearly visible in both maps, the R(280 nm) map appears to be less sharp, despite having the same spatial resolution as the R(550 nm) map. We believe this blurring is because of increased scattering at 280 nm and that some of the scattered light is lost via the 0.3 mm gap between the integrating sphere and the wafer surface, thus reducing the signal-to-noise ratio. The corresponding EAF maps, calculated using the correlation fits from Fig. 5, are presented on the same scale in Fig. 6(c) and (d). The EAF map determined from R(280 nm) clearly exhibits more regions with higher EAF values (and some with lower values) compared with the map determined using R(550 nm).

The corresponding variability plot for the EAF maps shown in Fig. 6(c) and (d) is shown in Fig. 7(a). The median EAF values determined from both methods show good agreement. However, the R(550 nm) method detects no EAF values above ∼1.9, whereas the R(280 nm) method detects a significant number of data points above this level. Fig. 7(b) shows the EAF values for four different locations on the same wafer versus EAF as
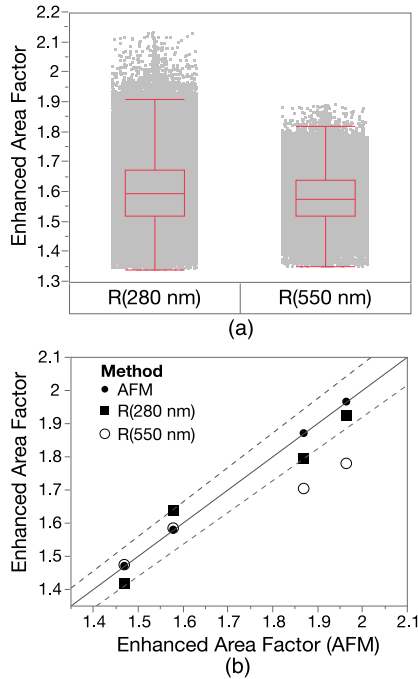
Fig. 7.   (a) Variability plots for the EAF maps shown in Fig. 6(c) and (d) for texture condition MCCE-M2. (b) EAF values for four different locations on the same wafer versus EAF as measured with AFM, with employed methods indicated. The dotted lines indicate 4% deviation from the AFM values.
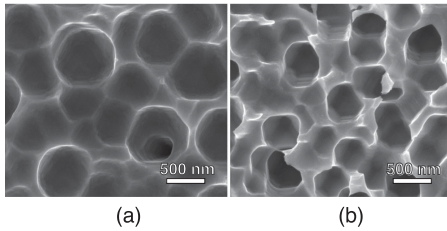

Fig. 8.   Plan-view SEM images for textures (a) MCCE-M1 and (b) MCCE-M2.

measured by AFM, with the three employed methods indicated. The solid line corresponds to the AFM results and the dotted lines indicate a 4% deviation from these values. The R(280 nm) EAF values show good agreement with the AFM results, with all values falling within 4%. The R(550 nm) EAF values exhibit excellent agreement with AFM for the two lower EAF values but poor agreement for the two higher EAF values. The results in Fig. 7 indicate that while R(550 nm) mapping could be used to monitor relative changes in median EAF values, it is unsuitable to monitor spatial variation in EAF. Furthermore, while the results in Fig. 5 suggested that R(280 nm) would be better suited for higher EAF values, we see in Fig. 7, that it exhibits better accuracy even for a relatively low EAF value of 1.9.

C. Monitoring Texture Variation and Impact on Diffusion

Fig. 8(a) and (b) shows plan-view SEM images for the two MCCE texture conditions applied to "sistered" mc-Si wafers, MCCE-M1 and MCCE-M2, respectively. MCCE-M2 (shorter post-nano-pitting etch-back time) exhibits a higher density of
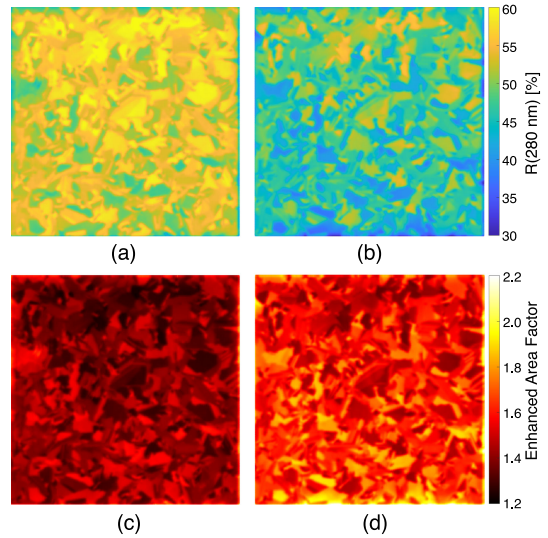

Fig. 9.   R(280 nm) maps (154.75 mm by 154.75 mm) of "sistered" multicrystalline wafers with texture conditions (a) MCCE-M1 and (b) MCCE-M2 presented on the same scale. The corresponding EAF maps, (c) and (d), are shown directly below them and presented on the same scale.

inverted features with smaller openings compared with MCCC-M1.

The corresponding full-wafer R(280 nm) maps for MCCE-M1 and MCCE-M2 are shown, on the same scale, in Fig. 9(a) and (b), respectively. The R(280 nm) map for MCCE-M2 exhibits an overall lower reflectance compared with MCCE-M1. The corresponding EAF maps, calculated using the exponential decay fit from Fig. 5(a), are shown, on the same scale, in Fig. 9(c) and (d). The overall EAF values are higher for the MCCE-M2 condition and the significant change for specific (nominally identical) grains is apparent.

Post-diffusion sheet resistance versus R(280 nm) and EAF (at the same nominal locations) for the MCCE-M1 and MCCE-M2 conditions are shown in Fig. 10(a) and (b), respectively. There is a clear increase in sheet resistance with increasing R(280 nm) values and a corresponding decrease with increasing EAF. There is also a clear offset in sheet resistance between the two different textures. The trend in Fig. 10(b) is consistent with our previous study where sheet resistance decreased for MCCE textures, which exhibited both increasing EAF and surface-to-volume ratio [11]. Note that for different morphologies, sheet resistance can increase with increasing EAF [11]. The results in Fig. 10 confirm that R(280 nm) mapping provides sufficient sensitivity to monitor the impact of both the nanotexture spatial variation across a wafer and the variation between texture conditions on phosphorus diffusion. We suggest that R(280 nm) mapping may be extended to spatial variation studies for other parameters, like those related to recombination for example.

D. FDTD Simulations of R(E2) Versus EAF

Fig. 11(a) shows the calculated EAF versus VPA for the nanopyramid conditions selected for FDTD simulations, with height values (fixed for the vertical groups) and slant angles indicated. This matrix of conditions covers a fuller range of EAF versus VPA compared with the linear relation suggested
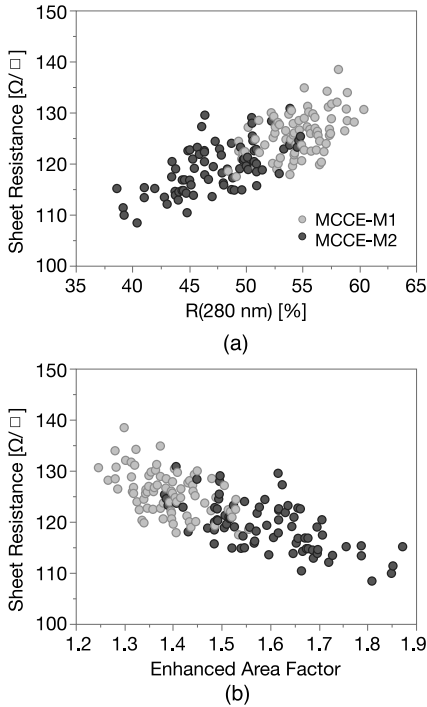
Fig. 10.   (a) Sheet resistance versus R(280 nm), both measured at the same wafer locations, for MCCE-M1 and MCCE-M2. (b) Corresponding plot for sheet resistance versus EAF.
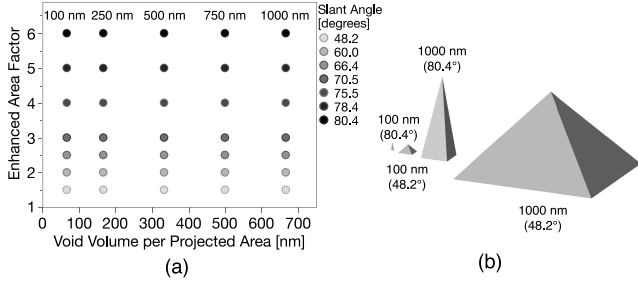

Fig. 11.   (a) EAF versus VPA for the 35 nanopyramid FDTD simulation conditions with the corresponding heights (vertical groups) and slant angles indicated. (b) Schematics of some unit cells (without substrate), shown on the same scale, with heights and slant angles indicated.

Fig. 12.   (a) Simulated R(E2) peaks for the nanopyramid conditions with 100 nm heights. (b) R(E2) peak values versus EAF for all the simulated conditions along with an exponential fit and 95% CI prediction bounds. The fit to the experimental data from Fig. 5 is also shown for reference.

35 conditions. Significant shifts in the R(E2) peak position have also been reported for porous silicon [21] and for silicon-on-sapphire [37]. While those peak shifts appeared to be related to varying porosity and void gradients, the underlying mechanism is unclear. The peak shifts observed here with the nanopyramid simulations also require further investigation. The R(E2) peak values versus EAF for all the simulated conditions are shown in Fig. 12(b) along with an exponential fit and 95% confidence interval (CI) prediction bounds. The fit to the experimental data from Fig. 5(a) is also shown for reference. The simulated R(E2) results exhibit a general decay with increasing EAF, but with a fairly wide "decay band." The R(E2) results exhibit larger variation for EAF below 5 with the largest variation at 1.5. The general decay trend in Fig 12(b) is consistent with the measured R(E2) trend shown in Fig. 5(a). The fit to the experimental data also falls within the 95% CI prediction bounds of the exponential fit to the FDTD results. The wide "decay band" suggests that it is plausible for nanotextures with dissimilar morphologies to fall on the same decay curve, as observed for the MCCE and RIE conditions in Fig. 5(a). However, the wide "decay band" also suggests that the specific exponential decay exhibited collectively by the MCCE and RIE conditions is an empirical relationship specific to the textures investigated here and does not represent a "universal" or general relation applicable to any nanotexture. We also note that the simulated textures are perfectly ordered periodic arrays of ideal nanopyramids and, as such, do not fully capture the impact of morphology changes and of randomly distributed features on R(E2). While the simulations support the general trend observed for the experimental results, further study is required to better understand the underlying relationship between R(E2) and EAF for nanotextures.

IV. CONCLUSION

In this article, we presented a clear empirical decay correlation between R(E2) and EAF for multiple silicon nanotexture conditions prepared with MCCE and RIE. We extended this

by the RIE AFM results of Fig. 4(b). Schematics of some of the nanopyramid conditions are shown in Fig. 11(b) to illustrate the range of features. The goal of simulating such a wide range of texture features with multiple conditions having the same EAF is to verify, at least to a first order, the decay relation between R(E2) and EAF and also to investigate the extent of data spread in the relationship. We also wish to gauge if the extent of the spread is consistent with the MCCE and RIE conditions falling on the same decay curve as shown in Fig. 5(a).

The simulated R(E2) peaks for the nanopyramid conditions with heights of 100 nm are shown in Fig. 12(a), where the R(E2) peak is decreasing with increasing EAF. This general trend was observed for all height groups. We also note that the position of the R(E2) peak varied between 265 and 285 nm across the
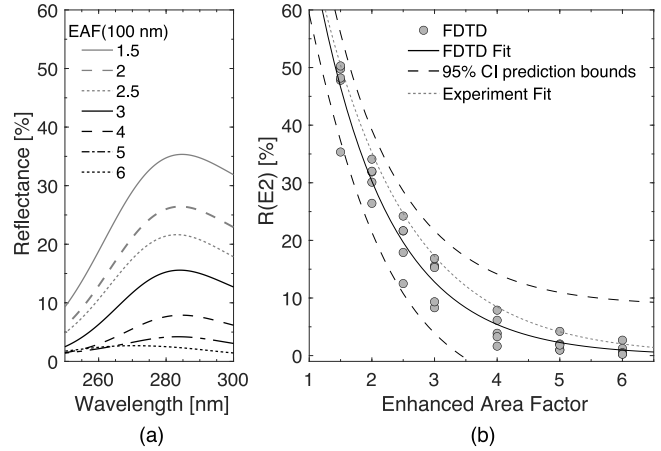
correlation to R(280 nm) mapping and demonstrated accurate, high-resolution EAF spatial mapping of full-sized nanotextured wafers. As an application example, R(280 nm) mapping was shown to provide sufficient sensitivity to monitor the impact of both the nanotexture spatial variation across a wafer and the variation between texture conditions on post-diffusion sheet resistance. FDTD simulations of several nanopyramid conditions spanning a wide range of EAF and VPA values yielded a decay band for R(E2) versus EAF, consistent with our experimental results. Despite the potential difficulties of creating an R(E2) versus EAF correlation curve, we propose that when investigating samples prepared within a given texture process or subjected to process variations within the same texture method, an R(E2) map on its own will be sufficient to detect and monitor relative spatial variation in nanotexture EAF. We suggest that R(E2) mapping may prove useful for correlating texture variation with other properties like recombination-related parameters and for other nanotextured silicon applications where enhanced surface area is critical.

ACKNOWLEDGMENT

REFERENCES

[1] J. R. Szczech and S. Jin, "Nanostructured silicon for high capacity lithium battery anodes," *Energy Environ. Sci.*, vol. 4, no. 1, pp. 56–72, 2011.

[2] M. Ge, X. Fang, J. Rong, and C. Zhou, "Review of porous silicon preparation and its application for lithium-ion battery anodes," *Nanotechnology*, vol. 24, no. 42, Sep. 2013, Art. no. 422001.

[3] J. Oh, T. G. Deutsch, H.-C. Yuan, and H. M. Branz, "Nanoporous black silicon photocathode for H_2 production by photoelectrochemical water splitting," *Energy Environ. Sci.*, vol. 4, no. 5, pp. 1690–1694, 2011.

[4] I. Oh, J. Kye, and S. Hwang, "Enhanced photoelectrochemical hydrogen production from silicon nanowire array photocathode," *Nano Lett.*, vol. 12, no. 1, pp. 298–302, Jan. 11, 2012.

[5] X. Liu *et al.*, "Black silicon: Fabrication methods, properties and solar energy applications," *Energy Environ. Sci.*, vol. 7, no. 10, pp. 3223–3263, 2014.

[6] M. Otto *et al.*, "Black silicon photovoltaics," *Adv. Opt. Mater.*, vol. 3, no. 2, pp. 147–164, 2015.

[7] J. Oh, H.-C. Yuan, and H. M. Branz, "An 18.2%-efficient black-silicon solar cell achieved through control of carrier recombination in nanostructures," *Nat. Nanotechnol.*, vol. 7, no. 11, pp. 743–748, Nov. 2012.

[8] P. Li *et al.*, "Effective optimization of emitters and surface passivation for nanostructured silicon solar cells," *RSC Adv.*, vol. 6, no. 106, pp. 104073–104081, 2016.

[9] S. Zhong *et al.*, "Influence of the texturing structure on the properties of black silicon solar cell," *Sol. Energy Mater. Sol. Cells*, vol. 108, pp. 200–204, Jan. 2013.

[10] B. Kafle *et al.*, "On the emitter formation in nanotextured silicon solar cells to achieve improved electrical performances," *Sol. Energy Mater. Sol. Cells*, vol. 152, pp. 94–102, Aug. 2016.

[11] G. Scardera *et al.*, "On the enhanced phosphorus doping of nanotextured black silicon," *IEEE J. Photovolt.*, vol. 11, no. 2, pp. 298–305, Mar. 2021.

[12] F. Wu *et al.*, "Suppression of surface and Auger recombination by formation and control of radial junction in silicon microwire solar cells," *Nano Energy*, vol. 58, pp. 817–824, Apr. 2019.

[13] X. Dai *et al.*, "The influence of surface structure on diffusion and passivation in multicrystalline silicon solar cells textured by metal assisted chemical etching (MACE) method," *Sol. Energy Mater. Sol. Cells*, vol. 186, pp. 42–49, Nov. 2018.

[14] T. P. Pasanen, H. S. Laine, V. Vähänissi, J. Schön, and H. Savin, "Black silicon significantly enhances phosphorus diffusion gettering," *Sci. Rep.*, vol. 8, no. 1, Jan. 2018, Art. no. 1991.

[15] Z. Shen *et al.*, "Black silicon on emitter diminishes the lateral electric field and enhances the blue response of a solar cell by optimizing depletion region uniformity," *Scripta Materialia*, vol. 68, no. 3, pp. 199–202, Feb. 2013.

[16] H. R. Philipp and E. A. Taft, "Optical constants of silicon in the region 1 to 10 ev," *Phys. Rev.*, vol. 120, no. 1, pp. 37–38, Oct. 1960.

[17] M. A. Green, "Self-consistent optical parameters of intrinsic silicon at 300K including temperature coefficients," *Sol. Energy Mater. Sol. Cells*, vol. 92, no. 11, pp. 1305–1310, Nov. 2008.

[18] M. Welkowsky and R. Braunstein, "Interband transitions and exciton effects in semiconductors," *Phys. Rev. B*, vol. 5, no. 2, pp. 497–509, Jan. 1972.

[19] P. J. Zanzucchi and M. T. Duffy, "Surface damage and the optical reflectance of single-crystal silicon," *Appl. Opt.*, vol. 17, no. 21, pp. 3477–3481, Nov. 1978.

[20] G. E. Jellison, "Optical functions of silicon determined by two-channel polarization modulation ellipsometry," *Opt. Mater.,* vol. 1, no. 1, pp. 41–47, Jan. 1992.

[21] W. Theiß, "Optical properties of porous silicon," *Surf. Sci. Rep.*, vol. 29, no. 3, pp. 91–192, Jan. 1997.

[22] M. A. Green, *Silicon Solar Cells: Advanced Principles & Practice*. Kensington, NSW, Australia: Centre Photovolt. Devices Syst., 1995.

[23] C. Kühl, H. Schlötterer, and F. Schwidefsky, "Optical investigation of different silicon films," *J. Electrochem. Soc.*, vol. 121, no. 11, pp. 1496–1500, 1974.

[24] J. R. Chelikowsky and M. L. Cohen, "Nonlocal pseudopotential calculations for the electronic structure of eleven diamond and zinc-blende semiconductors," *Phys. Rev. B*, vol. 14, no. 2, pp. 556–582, Jul. 1976.

[25] G. Harbeke, "Assessment of the surface quality of SIMOX wafers by UV reflectance," *J. Electrochem. Soc.*, vol. 137, no. 2, pp. 696–699, 1990.

[26] C.-Y. Tsai, "Absorption coefficients of silicon: A theoretical treatment," *J. Appl. Phys.*, vol. 123, no. 18, 2018, Art. no. 183103.

[27] M. T. Duffy *et al.*, "Measurement of the near-surface crystallinity of silicon on sapphire by UV reflectance," *J. Cryst. Growth*, vol. 58, no. 1, pp. 10–18, Jun. 1982.

[28] A. Straub *et al.*, "Fast and non-destructive assessment of epitaxial quality of polycrystalline silicon films on glass by optical measurements," *J. Cryst. Growth*, vol. 265, no. 1, pp. 168–173, Apr. 2004.

[29] Y. Xia, B. Liu, S. Zhong, and C. Li, "X-ray photoelectron spectroscopic studies of black silicon for solar cell," *J. Electron Spectrosc. Related Phenomena*, vol. 184, no. 11, pp. 589–592, Jan. 2012.

[30] D. E. Aspnes, "Optical properties of thin films," *Thin Solid Films*, vol. 89, no. 3, pp. 249–262, Mar. 1982.

[31] S. Zou *et al.*, "Complementary etching behavior of alkali, metal-catalyzed chemical, and post-etching of multicrystalline silicon wafers," *Prog. Photovolt., Res. Appl.*, vol. 27, no. 6, pp. 511–519, 2019.

[32] P. Klapetek, D. Necas, and C. Anderson, "Gwyddion user guide," 2012. [Online]. Available: http://gwyddion.net/documentation/user-guide-en

[33] N. David and K. Petr, "Gwyddion: An open-source software for SPM data analysis," *Open Phys.*, vol. 10, no. 1, pp. 181–188, 2012.

[34] B. Bhushan, "Surface roughness analysis and measurement techniques," in *Modern Tribology Handbook, Two Volume Set*. Boca Raton, FL, USA: CRC Press, 2001, ch. 2.2.2.4.

[35] C. C. Striemer and P. M. Fauchet, "Dynamic etching of silicon for broadband antireflection applications," *Appl. Phys. Lett.*, vol. 81, no. 16, pp. 2980–2982, 2002.

[36] Y. Zhang *et al.*, "3D characterisation using plasma FIB-SEM: A large-area tomography technique for complex surfaces like black silicon," *Ultramicroscopy*, vol. 218, Nov. 2020, Art. no. 113084.

[37] C. Pickering *et al.*, "Interpretation of UV reflectance measurements on silicon-on-sapphire by spectral reflectance and spectroscopic ellipsometry studies," *MRS Proc.*, vol. 53, 1985, Art. no. 317.